To be published in Optics Letters:

Title:	Extending the range of distributed fiber optic
Authors:	Daniel Sweeney,Christian Petrie
Accepted:	12 November 21
Posted	12 November 21
DOI:	https://doi.org/10.1364/OL.445245

© 2021 Optica

OPTICA
PUBLISHING GROUP
Formerly OSA

Expanding the range of resolvable strain from distributed fiber optic sensors using a local adaptive reference approach

DANIEL C. SWEENEY[1,*] AND CHRISTIAN M. PETRIE[1]

[1] Advanced Fuel Fabrication and Instrumentation Group, Oak Ridge National Laboratory, 1 Bethel Valley Road, Oak Ridge, TN 37831
[*] Corresponding author: sweeneydc@ornl.gov

Compiled November 9, 2021

Optical frequency domain reflectometry (OFDR) is a spectral measurement technique in which shifts in the local Rayleigh backscatter spectra can be used to perform distributed temperature or strain measurements relative to a reference measurement using ordinary singlemode optical fibers. This work demonstrates a data processing methodology for improving the resolvable range of temperature and strain by adaptively varying the reference measurement position by position, based on the time evolution of the local optical intensities and the correlation between the reference and active measurements. These methods nearly double the resolvable range of temperature and strain compared to that achieved using the traditional static reference approach.

© 2021 Optical Society of America

OCIS codes: (290.5870) Scattering, Rayleigh; (060.2430) Fibers, singlemode; (070.2025) Discrete optical signal processing; (200.4560) Optical data processing.

http://dx.doi.org/10.1364/ao.XX.XXXXXX

1. INTRODUCTION

Distributed optical fiber–based sensors (DOFSs) are an attractive option for measuring strain and temperature in industrial environments because they can be interrogated remotely, are immune to electromagnetic interference, have a small footprint, and can provide high resolution (micrometer to meter) measurements over long distances (meters to kilometers). DOFSs leverage the spatially dependent backscattering of light and are generally categorized by their interrogation technique, such as optical time domain reflectometry (OTDR) and optical frequency domain reflectometry (OFDR), and light scattering mechanism (e.g., Rayleigh, Raman, and Brillouin scattering) [1]. DOFS systems based on optical frequency domain reflectometry (OFDR) are particularly attractive because they can achieve sub-centimeter spatial resolution using conventional singlemode telecommunication fibers as the sensor [2]. Commercially available OFDR instruments, such as the OBR-4600 (OBR; Luna Innovations, Inc., Blacksburg, VA, USA), use a tunable laser source (TLS) to interrogate a fiber under test (FUT) measuring tens of meters in length, which is either bonded to the surface of a component to measure strain or left unconstrained to measure temperature. Rayleigh backscatter along the FUT interferes with light transmitted through a reference fiber (Fig. 1). The interference patterns are monitored by two photodiodes after being split into s- and p-polarization states to resolve the frequency-domain interference pattern. The interference pattern is then transformed into the time-of-flight domain and subdivided into small, sub-millimeter segments that are referred to as sensors. These sensors are analyzed individually to enable distributed measurements. This configuration is depicted in Fig. 1, in which a sensor is shown in blue. As the figure shows, the sensor is only a small part of the overall FUT.

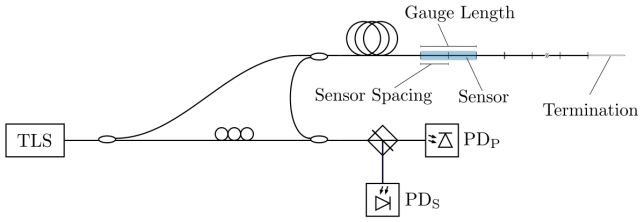

Fig. 1. Simplified schematic of an OFDR system.

The success of DOFSs has motivated interest in their use under more extreme conditions, such as exposure to higher strains and temperatures, radiation fields, and corrosive environments. Silica-based optical fibers have a fictive temperature of approximately 1,700°C [3], devitrify gradually at temperatures > 1000°C [4], are strong under tension, and have shown acceptable transmission after exposure to moderate ionizing radiation dose [5, 6]. In addition, many previous works have attempted to embed optical fibers within a wide range of polymers [7, 8], metals [9–11], and ceramics [12, 13] to provide distributed strain measurements for structural health monitoring. However,

[1] This manuscript has been authored by UT-Battelle, LLC, under contract DE-AC05-00OR22725 with the US Department of Energy (DOE). The US government retains and the publisher, by accepting the article for publication, acknowledges that the US government retains a nonexclusive, paid-up, irrevocable, worldwide license to publish or reproduce the published form of this manuscript, or allow others to do so, for US government purposes. DOE will provide public access to these results of federally sponsored research in accordance with the DOE Public Access Plan (http://energy.gov/downloads/doe-public-access-plan).

in addition to risking the fiber's survival during fabrication, this is especially challenging for fibers embedded within metals. This is because the metals have a significantly higher thermal expansion coefficient compared to fiber, which results in large fiber strains at high temperatures. In these cases, as long as the the fiber transmission is not significantly impacted by the large thermal strain, it is hypothesized that the inability to resolve such large strains could be rectified using adaptive signal processing techniques.

Several approaches have been proposed to improve the correlation between active and reference OFDR measurements. For example, previous works have demonstrated that temperature and strain can be resolved from an OFDR data set using a cumulative sum of differential measurements [7] or by training a neural network to detect changes in the optical spectra [14]. Other methods have been suggested, but they are focused on the point-removal of non-physical data [15, 16]. Recently, Sweeney et al. published a post-processing method to extend the range of existing OFDR measurements to temperatures beyond 950°C and during nuclear reactor exposure to neutron fluences in excess of 10^{18} n/cm^2 [17, 18]. This method—referred to as the *inchworm method*—accounts for slow changes in the random density fluctuations that establish the Rayleigh backscatter signature of a given FUT by adaptively varying the reference scan based on the correlation between the reference scan and the active scan. Temperature and strain measurements can be calculated by summing incremental multiple relative measurements which are ultimately linked back to the initial reference scan.

In a previous work, Petrie et al. embedded a copper-coated optical fiber in aluminum using ultrasonic additive manufacturing [9]. Although the embedded fiber survived heating to temperatures of ∼ 500°C, the strain within the embedded region relative to the initial strain at room temperature could no longer be resolved shortly after reaching 500°C. When the inchworm algorithm was used to analyze the same data, some improvement in the resolvable strain was observed at lower temperatures, but the strain still could not be resolved when the temperature was increased to 500°C [17]. To address these challenges, this letter proposes a modification to the inchworm algorithm that uses the same adaptive reference approach to evaluate each spatial subdivision of the fiber, thus allowing the reference to be varied independently for each location. This sensor-by-sensor adaptive reference approach is demonstrated for the aforementioned data set, but it is expected to be more generally applicable for a wider range of harsh environment strain monitoring applications.

2. METHODS

Building on the initial work of Froggatt and Moore [2], OFDR data were analyzed using a process analogous to a sliding bandpass filter. The photodetectors shown in Fig. 1 record optical intensities as a function of optical frequency, which is varied using the TLS. After performing a discrete Fourier transform, the Rayleigh backscatter profile $R(t,x)$ recorded at time t can be represented as a function of axial position along the fiber x. This spatial distribution is divided into n segments—referred to as *sensors*—with a spatial width Δx and center position x_n, as represented by the shaded bar in Fig. 2(a). The discrete inverse Fourier transform of each segment, over the optical frequencies ν supported by the TLS, yields the optical spectrum of each sensor (Fig. 2b). This operation is given

$$I_n(t,\nu) = \mathcal{F}_\nu^{-1}\{[R(t,x)]_n\}, \tag{1}$$

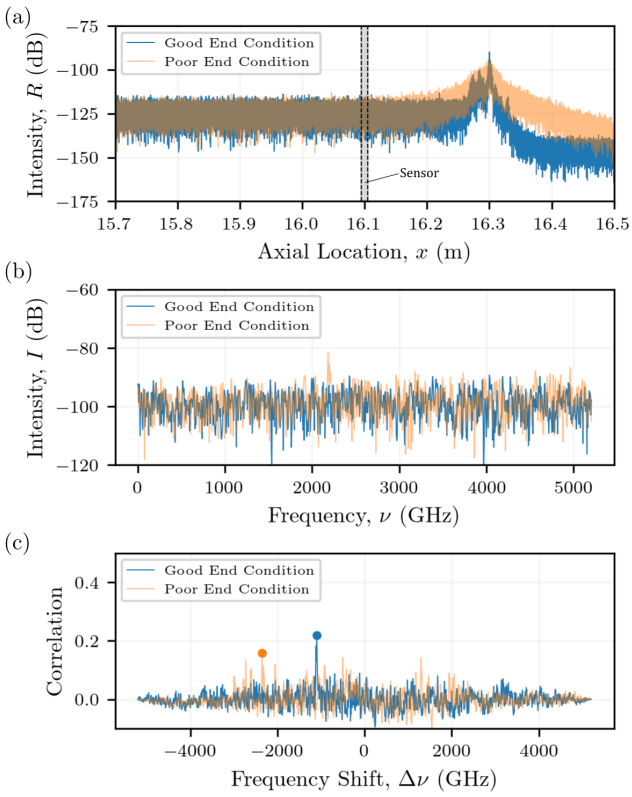

Fig. 2. (a) Spatially distributed Rayleigh backscatter profile from an FUT with the shaded region representing a single sensor, (b) transformed into the ν-domain, and (c) cross-correlated with a reference scan.

where $\mathcal{F}_\nu^{-1}\{\cdot\}$ is the discrete inverse Fourier transform over the range of the TLS [2], and $[\cdot]_n$ represents the windowing function over the spatial range of sensor n. This process is analogous to a discrete bandpass filter, which is used to isolate the optical frequency content associated with sensor n.

For each spatial position, the ν-domain intensity spectra for an active scan $I_n(t_a,\nu)$ and a reference scan $I_n(t_r,\nu)$ are then cross-correlated to calculate the spectral shift between them. To mitigate the identification of false peaks in the cross-correlation, the mean (over all ν) intensity of $I_n(t,\nu)$ is subtracted: $I_n'(t,\nu) = I_n(t,\nu) - \bar{I}_n(t,\nu)$. The normalized complex cross-correlation operation is then performed:

$$\chi_n(t_a,t_r) = \frac{I_n'(t_a,\nu)}{\|I_n'(t_a,\nu)\|} \otimes \frac{I_n'(t_r,\nu)}{\|I_n'(t_r,\nu)\|}, \tag{2}$$

where $\|\cdot\|$ is the L^2-norm (standard deviation). The spectral shift $\Delta\nu_n(t_a,t_0)$ of the active scan at time t_a, relative to the initial scan at time t_0, is calculated through the cumulative summation

$$\Delta\nu_n(t_a,t_0) = \underset{\nu}{\operatorname{argmax}}\{\chi_n(t_a,t_r)\} + \Delta\nu_n(t_r,t_0). \tag{3}$$

Then, $\Delta\nu_n(t_a,t_0)$ can be related to the local temperature and/or strain in the FUT according to the following equation:

$$\Delta\nu(t_a,t_r) = \nu_0\Big(K_\varepsilon\Delta\varepsilon(t_a,t_r) + K_T\Delta T(t_a,t_r)\Big), \tag{4}$$

where K_ε is the strain calibration coefficient (photoelastic contributions), and K_T is the temperature calibration coefficient

(thermo-optic and thermal expansion contributions). The cross-correlation operation is critical to correctly determining $\Delta\nu_n(t_a, t_0)$. The strength of the correlation, or quality $Q_n(t_a, t_r)$, is characterized by the height of its peak:

$$Q_n(t_a, t_r) = \max\{\chi_n(t_a, t_r)\}. \quad (5)$$

A quality heuristic threshold of $Q_{th} \geq 0.15$ has been previously suggested for identifying good correlations [16–18]. Sweeney et al. used spectral shift quality alone in their initial presentation of the inchworm algorithm.

3. RESULTS

Data from a copper-coated optical fiber, originally embedded in an aluminum block and heated to 500°C by Petrie et al. [9], are shown in Fig. 2. A short length of termination fiber (a coreless fiber) was spliced to the end of the FUT to prevent end reflections from interfering with the sensing measurements near the end of the fiber. However, Fig. 2(a) shows how this end condition is affected during the test and broadens the peak at 16.3 m intermittently. Spectral content from the poor end condition dominates the spectral content of the desired Rayleigh backscattered light upstream of the end condition (such as at 16.1 m). This alters the interference patterns in the ν-domain (Fig. 2(b)), which results in the identification of a false cross-correlation peak. The false peak then affects the measurements of $\Delta\nu_n(t_a, t_0)$ and $Q_n(t_a, t_r)$.

Because the inchworm algorithm uses $Q_n(t_a, t_r)$ as a metric for determining an appropriate reference measurement, false cross-correlation peaks produce non-physical temperature and strain measurements. As such, it is desirable to isolate scans with significant spectral crosstalk between adjacent sensors during post-processing to mitigate the propagation of these artifacts. One solution is to determine the relative difference of the average spatial intensities $\Lambda_n(t_a, t_r)$ of the active and reference scans at the same sensor location. This parameter can be used in addition to quality to aid in the selection of the best pairing of target and reference scans. The parameter $\Lambda_n(t_a, t_r)$ is calculated as

$$\Lambda_n(t_a, t_r) = \frac{|\bar{I}_n(t_a, x) - \bar{I}_n(t_r, x)|}{\bar{I}_n(t_r, x)}. \quad (6)$$

In addition to using this parameter, the inchworm algorithm [17] can also be modified to operate on a sensor-by-sensor basis, as shown in Fig. 3. This modification retains the advantage of the inchworm algorithm in that error is only propagated when required to provide an improved reference for an active scan. In Fig. 3, the algorithm independently analyzes each sensor position x_n, starting with $n = 0$, for each recorded spectrum taken at times $0 \leq t \leq T$. The active scan is advanced to t_1 (i.e., $a = 1$), cross-correlated with the scan at t_0, and $\Delta\nu_n(t_a, t_0)$, $Q_n(t_a, t_r)$, $\Lambda_n(t_a, t_r)$ are calculated. If $Q_n(t_a, t_r) \geq Q_{th}$, then the calculated values for $\Delta\nu_n(t_a, t_0)$, $Q_n(t_a, t_r)$, $\Lambda_n(t_a, t_r)$ are stored, and the process is repeated after incrementing a. This process is repeated until the last scan t_T, at which point the next spatial position is analyzed. If $Q_n(t_a, t_r) < Q_{th}$, then the reference scan t_r is set to the scan immediately prior to t_a and is iterated in reverse until $t_r = t_0$ or this criterion is met. If $Q_n(t_a, t_0) < Q_{th}$, the scan is not used as a reference for future scans.

Processing the data from the UAM-embedded Cu-coated fiber using a static reference ($t_r = t_0$) successfully reconstructs $\Delta\nu_n(t_a, t_0)$ within the embedded region (16.08 to 16.145 m) up until 175 min. After this time, a small portion of the embedded

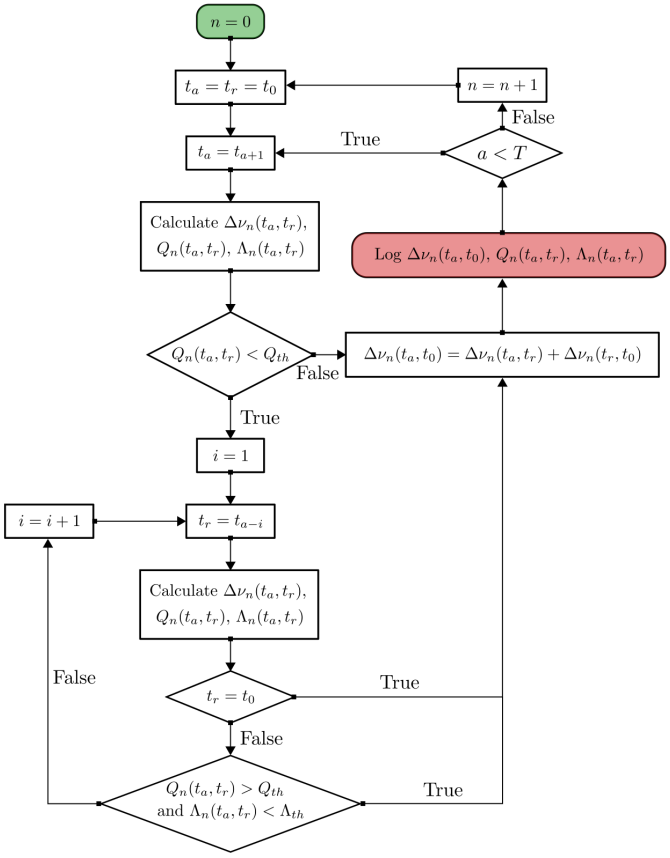

Fig. 3. Sensory-by-sensor inchworm algorithm flow chart.

region can still be resolved up to 300 min (Fig. 4a). With the sensor-by-sensor modified inchworm algorithm with $Q_{th} = 0.15$ and $\Lambda_{th} = 0.25$, individual aberrant scans appear, such as at 235 min. However, data between the reconstruction of $\Delta\nu_n(t_a, t_0)$ between 16.09 to 16.13 m, which comprises the majority of the embedded region, is much improved (Fig. 4b).

The sensor-by-sensor implementation of the inchworm algorithm improves reconstruction of $\Delta\nu_n(t_a, t_0)$ compared to the static reference method at the cost of two tuning parameters, Q_{th} and Λ_{th}, which require optimization. If Q_{th} is too high or if Λ_{th} is too low, then the inchworm analysis will yield similar results to the static reference analysis because the criteria to accept a reference scan as appropriate are too strict. Alternatively, if Q_{th} is too low or Λ_{th} is too high, then horizontal banding artifacts appear in the processed data, such as that which appears at 16.13 m at 250 min in Fig. 4(b). This banding occurs because the threshold is so widely met that it does not serve as a good metric to reject poor reference scans. However, 4 shows how the sensor-by-sensor inchworm algorithm can significantly improve reconstructions of $\Delta\nu_n(t_a, t_0)$ from embedded optical fibers at high temperatures when Q_{th} and Λ_{th} are appropriately selected.

Beyond improvements to data quality, the sensor-by-sensor inchworm analysis can be parallelized by analyzing each sensor n independently. The outer loop of Fig. 3, in which the sensor index n is incremented, can be performed for multiple sensors simultaneously, enabling a dramatic increase in analysis speed. Fig. 5 shows a comparison of the data from Fig. 4 analyzed using a static reference analysis, inchworm analysis as presented in [17, 18], and their threaded counterparts that analyzed 12 sensors simultaneously. At approximately 200 min, the runtime

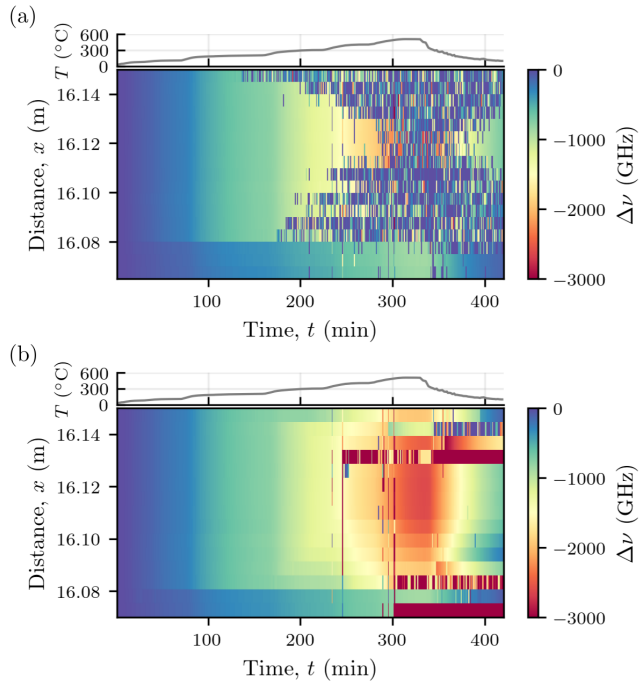

Fig. 4. (a) Static reference analysis and (b) sensor-by-sensor inchworm analysis ($Q_{th} = 0.15$, $\Lambda_{th} = 0.25$) of data from a metal-embedded FUT heated in steps up to 500°C.

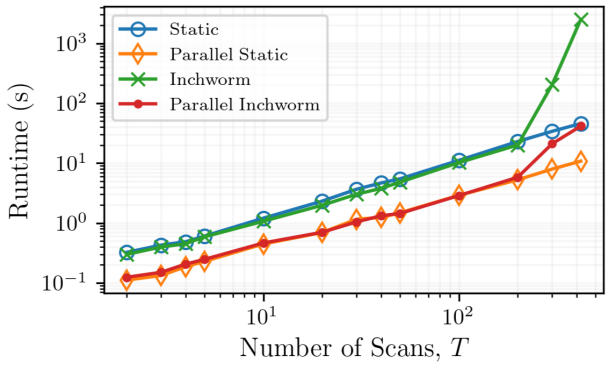

Fig. 5. Runtime efficiency using the static reference analysis, inchworm analysis ($Q_{th} = 0.15$), and the parallelized sensor-by-sensor inchworm analysis ($Q_{th} = 0.15$, $\Lambda_{th} = 0.25$).

of the inchworm analysis increases due to its adaptive nature. There is a similar but less prominent runtime increase in the parallelized sensor-by-sensor analysis, which ultimately has a shorter runtime by approximately three orders of magnitude while improving the $\Delta\nu_n(t_a, t_0)$ reconstruction. This advantage becomes even more important when analyzing larger data sets from FUTs exposed to harsh environments that require an adaptive reference scheme to successfully resolve $\Delta\nu_n(t_a, t_0)$.

4. DISCUSSION AND CONCLUSIONS

The ability to reliably deploy embedded optical fiber–based temperature and strain sensors for harsh environment distributed sensing applications requires robust data processing schemes to resolve $\Delta\nu_n(t_a, t_0)$, despite local changes to a sensor's Rayleigh backscatter profile or reductions in signal-to-noise ratios. The present work describes an adaptive reference method to resolve $\Delta\nu_n(t_a, t_0)$ beyond what is possible with conventional, static, reference-based methods. This algorithm is demonstrated using data from a metal-embedded optical fiber heated to temperatures up to 500°C (Fig. 4). The algorithm builds on the previous inchworm algorithm [17], which selects a reference that is most appropriate for all sensing positions for a given scan. The present sensor-by-sensor inchworm algorithm avoids poor-quality correlations between specific times for a specific sensor by decoupling the time histories for each individual sensor. Additionally, comparing the mean amplitude similarity (Λ_{th}) between scans can isolate sudden changes in the OFDR interference fringes to prevent the propagation of non-physical data. With these improvements, the sensor-by-sensor inchworm algorithm can enable distributed measurements of differential thermal strain in metal-embedded optical fibers up to 500°C using the naturally occurring density fluctuations in unmodified, standard singlemode telecommunication fiber. More generally, adaptive reference techniques such as the one presented herein could extend the operational range of distributed sensors utilizing Rayleigh backscatter in singlemode fiber beyond what is currently possible using naive post-processing methodologies.

Acknowledgements. This work was supported by the Transformational Challenge Reactor Program of the US Department of Energy, Office of Nuclear Energy.

Disclosures. The authors have a pending non-provisional patent application (application number 17/306,113) related to the present work that is currently under review by the US Patent and Trademark Office.

Data availability. Data underlying the results presented in this paper are available in Ref. [17].

REFERENCES

1. X. Bao and L. Chen, Sensors **12**, 8601 (2012).
2. M. Froggatt and J. Moore, Appl. Opt. **37**, 1735 (1998).
3. M. Tomozawa, J. Non-Crystalline Solids **286**, 132 (2001).
4. A. H. Rose, J. Light. Technol. **15**, 808 (1997).
5. G. Cheymol, H. Long, J. L. F. Villard, and B. Brichard, IEEE Transactions on Nucl. Sci. **55**, 2252 (2008).
6. C. M. Petrie, D. P. Hawn, W. Windl, and T. E. Blue, J. Non-Crystalline Solids **409**, 88 (2015).
7. S. Heinze and A. T. Echtermeyer, Appl. Sci. (Switzerland) **8** (2018).
8. V. Matveenko, I. Shardakov, A. Voronkov, N. Kosheleva, D. Lobanov, G. Serovaev, E. Spaskova, and G. Shipunov, Struct. Control. Heal. Monit. **25**, e2118 (2018).
9. C. M. Petrie, N. Sridharan, M. Subramanian, A. Hehr, M. Norfolk, and J. Sheridan, Smart Mater. Struct. **28**, 055012 (2019).
10. C. M. Petrie, N. Sridharan, A. Hehr, M. Norfolk, and J. Sheridan, Smart Mater. Struct. **28**, 085041 (2019).
11. D. Havermann, J. Mathew, W. N. MacPherson, R. R. Maier, and D. P. Hand, J. lightwave technology **33**, 2474 (2014).
12. A. Ghazanfari, W. Li, M. C. Leu, Y. Zhuang, and J. Huang, Mater. & Des. **112**, 197 (2016).
13. C. M. Petrie, A. M. Schrell, D. N. Leonard, Y. Yang, B. C. Jolly, and K. A. Terrani, J. Nucl. Mater. p. 153012 (2021).
14. J. Sierra-Pérez, M. A. Torres-Arredondo, and A. Güemes, Compos. Struct. **135**, 156 (2016).
15. M. L. Luo, J. Liu, C. Tang, X. Wang, T. Lan, and B. Kan, Opt. Express **27**, 35823 (2019).
16. M. F. Bado, J. R. Casas, and J. Gómez, Struct. Heal. Monit. **20**, 661 (2021).
17. D. C. Sweeney, A. M. Schrell, and C. M. Petrie, IEEE Sens. **21**, 498 (2021).
18. D. C. Sweeney, D. M. Sweeney, and C. M. Petrie, Sensors **21** (2021).

FULL REFERENCES

1. X. Bao and L. Chen, "Recent progress in distributed fiber optic sensors," Sensors **12**, 8601–8639 (2012).
2. M. Froggatt and J. Moore, "High-spatial-resolution distributed strain measurement in optical fiber with Rayleigh scatter," Appl. Opt. **37**, 1735–1740 (1998).
3. M. Tomozawa, "Fictive temperature of silica glass optical fibers—re-examination," J. Non-Crystalline Solids **286**, 132–138 (2001).
4. A. H. Rose, "Devitrification in annealed optical fiber," J. Light. Technol. **15**, 808–814 (1997).
5. G. Cheymol, H. Long, J. L. F. Villard, and B. Brichard, "High level gamma and neutron irradiation of silica optical fibers in CEA OSIRIS nuclear reactor," IEEE Transactions on Nucl. Sci. **55**, 2252–2258 (2008).
6. C. M. Petrie, D. P. Hawn, W. Windl, and T. E. Blue, "Reactor radiation-induced attenuation in fused silica optical fibers heated up to 1000 c," J. Non-Crystalline Solids **409**, 88–94 (2015).
7. S. Heinze and A. T. Echtermeyer, "A running reference analysis method to greatly improve Optical Backscatter Reflectometry strain data from the inside of hardening and shrinking materials," Appl. Sci. (Switzerland) **8** (2018).
8. V. Matveenko, I. Shardakov, A. Voronkov, N. Kosheleva, D. Lobanov, G. Serovaev, E. Spaskova, and G. Shipunov, "Measurement of strains by optical fiber bragg grating sensors embedded into polymer composite material," Struct. Control. Heal. Monit. **25**, e2118 (2018).
9. C. M. Petrie, N. Sridharan, M. Subramanian, A. Hehr, M. Norfolk, and J. Sheridan, "Embedded metallized optical fibers for high temperature applications," Smart Mater. Struct. **28**, 055012 (2019).
10. C. M. Petrie, N. Sridharan, A. Hehr, M. Norfolk, and J. Sheridan, "High-temperature strain monitoring of stainless steel using fiber optics embedded in ultrasonically consolidated nickel layers," Smart Mater. Struct. **28**, 085041 (2019).
11. D. Havermann, J. Mathew, W. N. MacPherson, R. R. Maier, and D. P. Hand, "Temperature and strain measurements with fiber bragg gratings embedded in stainless steel 316," J. lightwave technology **33**, 2474–2479 (2014).
12. A. Ghazanfari, W. Li, M. C. Leu, Y. Zhuang, and J. Huang, "Advanced ceramic components with embedded sapphire optical fiber sensors for high temperature applications," Mater. & Des. **112**, 197–206 (2016).
13. C. M. Petrie, A. M. Schrell, D. N. Leonard, Y. Yang, B. C. Jolly, and K. A. Terrani, "Embedded sensors in additively manufactured silicon carbide," J. Nucl. Mater. p. 153012 (2021).
14. J. Sierra-Pérez, M. A. Torres-Arredondo, and A. Güemes, "Damage and nonlinearities detection in wind turbine blades based on strain field pattern recognition. fbgs, obr and strain gauges comparison," Compos. Struct. **135**, 156–166 (2016).
15. M. L. Luo, J. Liu, C. Tang, X. Wang, T. Lan, and B. Kan, "0.5 mm spatial resolution distributed fiber temperature and strain sensor with position-deviation compensation based on OFDR," Opt. Express **27**, 35823–35829 (2019).
16. M. F. Bado, J. R. Casas, and J. Gómez, "Post-processing algorithms for distributed optical fiber sensing in structural health monitoring applications," Struct. Heal. Monit. **20**, 661–680 (2021).
17. D. C. Sweeney, A. M. Schrell, and C. M. Petrie, "An Adaptive Reference Scheme to Extend the Functional Range of Optical Backscatter Reflectometry in Extreme Environments," IEEE Sens. **21**, 498–509 (2021).
18. D. C. Sweeney, D. M. Sweeney, and C. M. Petrie, "Graphical optimization of spectral shift reconstructions for optical backscatter reflectometry," Sensors **21** (2021).

OPTICA PUBLISHING GROUP For OPTICA